



HAL
open science

Toward Huygens' sources with dodecahedral plasmonic clusters

Laurent Lermusiaux, Véronique Many, Philippe Barois, Virginie Ponsinet, Serge Ravaine, Etienne Duguet, Mona Tréguer-Delapierre, Alexandre Baron

► **To cite this version:**

Laurent Lermusiaux, Véronique Many, Philippe Barois, Virginie Ponsinet, Serge Ravaine, et al.. Toward Huygens' sources with dodecahedral plasmonic clusters. *Nano Letters*, 2021, 21 (5), pp.2046-2052. 10.1021/acs.nanolett.0c04666 . hal-03167125

HAL Id: hal-03167125

<https://hal.science/hal-03167125>

Submitted on 23 Mar 2021

HAL is a multi-disciplinary open access archive for the deposit and dissemination of scientific research documents, whether they are published or not. The documents may come from teaching and research institutions in France or abroad, or from public or private research centers.

L'archive ouverte pluridisciplinaire **HAL**, est destinée au dépôt et à la diffusion de documents scientifiques de niveau recherche, publiés ou non, émanant des établissements d'enseignement et de recherche français ou étrangers, des laboratoires publics ou privés.

Toward Huygens' sources with dodecahedral plasmonic clusters

Laurent Lermusiaux¹, Véronique Many^{1,2}, Philippe Barois², Virginie Ponsinet², Serge Ravaine², Etienne Dugue^{1†}, Mona Tréguer-Delapierre^{1*}, and Alexandre Baron^{2*}

¹⁾ Université de Bordeaux, CNRS, ICMCB, Bordeaux INP, UMR 5026, Pessac 33600, France; Present Address: Laboratoire de Chimie, CNRS, École Normale Supérieure de Lyon, 46 allée d'Italie, 69364 Lyon, France

²⁾ Université de Bordeaux, CNRS, CRPP, UMR 5031, Pessac 33600, France

Abstract: The design and chemical synthesis of plasmonic nanoresonators exhibiting a strong magnetic response in the visible is a key requirement to the realization of efficient functional and self-assembled metamaterials. However, novel applications like Huygens' metasurfaces or mu-near-zero materials require stronger magnetic responses than those currently reported. Our numerical simulations demonstrate that the specific dodecahedral morphology, whereby 12 silver satellites are located on the faces of a nanosized dielectric dodecahedron, provides sufficiently large electric and magnetic dipolar and quadrupolar responses that interfere to produce so-called generalized Huygens' sources, fulfilling the generalized Kerker condition. Using a multistep colloidal engineering approach, we synthesize highly symmetric plasmonic nanoclusters with a controlled silver satellite size and show that they exhibit a strong forward scattering that may be used in various applications such as metasurfaces or perfect absorbers.

The generation of artificial optical magnetism is a classical goal of the field of metamaterials. The vanishing of the magnetic susceptibility of natural materials for frequencies above gigahertz is well-known.⁽¹⁾ Nevertheless, it was a success of the emerging field of metamaterials to show that a strong local magnetization could be induced by an electromagnetic wave in artificial composites by an appropriate design of conducting elements embedded in an insulating dielectric matrix. The trick was to engineer subwavelength resonant inductor-capacitor circuits in which strong induced circular currents generate a magnetic dipole. Strictly speaking, the magnetization is induced by the electric field \mathbf{E} (or more precisely by its spatial variations as the curl of \mathbf{E}) unlike natural magnetic materials like paramagnets in which magnetic dipoles (spins) truly couple to the magnetic field. At microwave frequencies, the split-ring resonator design enabled the generation of a negative effective magnetic permeability.^(2,3) At higher frequencies of visible light, the size of the optical resonators should not exceed a few tens of nanometers, and plasmonic nanoparticles are good candidates for the realization of resonant optical devices. Several models of clusters of plasmonic nanoparticles have indeed been proposed⁽⁴⁻⁷⁾ for the generation of an intense magnetic polarization in response to visible light. Experimentally, the bottom-up approach has been successfully used to synthesize several types of magnetic clusters.⁽⁸⁻¹³⁾ Among them, the so-called "plasmonic raspberries" based on the Simovsky-Tretyakov model of magnetic nanoclusters⁽⁷⁾ have been extensively studied. Plasmonic raspberries consist of a corona of metallic nanospheres (gold or silver) evenly but randomly distributed at the surface of a dielectric core. The electric and magnetic contributions to their optical response have been unambiguously measured by light scattering experiments.^(10,12,13) It was found that the electric and magnetic dipolar resonances occur in the same frequency range and that the ratio of the two polarizations $R_{M/E}$ of the magnetic to electric dipolar scattering cross sections reaches 4.5%⁽¹²⁾ and 28%⁽¹³⁾ at resonance for gold and silver satellites, respectively. Moreover, a bulk metamaterial formed by a dense assembly of such silver raspberries exhibits non-natural values of the effective magnetic permeability ranging from 0.8 to 1.45 μ_0 .⁽¹³⁾ Novel applications like Huygens' metasurfaces⁽¹⁴⁾ or mu-near-zero materials⁽¹⁵⁾ require, however, a stronger magnetic response. For example, in the dipolar regime, the first Kerker condition for zero-backscattering requires equal values of the electric and magnetic dipole response ($R_{M/E} = 1$).^(16,17) In a recent publication, Elanchelian et al. demonstrated Huygens' scattering in the dipolar regime with spherical ensembles of large amounts of gold nano-inclusions arranged in emulsion droplets.⁽¹⁸⁾ In the multipolar regime, the so-called generalized Kerker (GK) condition is achieved when the superposition of symmetric (or even) multipoles is equal to that of odd multipoles.⁽¹⁹⁾ The odd/even parity is defined with respect to the radiated electric field distribution. Nanoresonators that reach the GK condition are also referred to as

generalized Huygens' sources and constitute key building blocks toward the realization of efficient functional metasurfaces such as metalenses,⁽²⁰⁾ beam deflectors,⁽²¹⁾ vortex plates,⁽²²⁾ holograms,⁽²³⁾ or perfect absorbers.⁽²⁴⁾

In an attempt to increase the magnetic polarizability, a more elaborated design was proposed in which a well-defined number of metallic satellites are located at the faces of platonic solids.⁽²⁵⁾ In a recent paper, we showed numerically that the dodecahedral morphology whereby 12 gold satellites are distributed on the faces of a nanosized dielectric dodecahedron is the most favorable, and the experimental study showed that $R_{M/E}$ is indeed increased by a factor 3 or more, compared to gold raspberries (from 4.5% to 14.5%).⁽²⁶⁾ This significant gain suggests that the dodecahedral morphology should be applied to silver satellites in order to surpass the silver-raspberry value of 28%. The goal of the present paper is to present the effect of the insertion of silver in the satellites of these highly symmetric dodecahedral clusters and demonstrate that they act as efficient forward scatterers.

The inset in Figure 1a is a typical rendition of the designed dodecahedral nanoclusters. It consists of a silica core of 45 nm in radius surrounded by silver satellites of 31.4 nm in radius positioned at the center of the 12 pentagonal faces of a dodecahedron (or equivalently on the vertices of a regular icosahedron) and spaced 0.5 nm from the silica core. The nanocluster is designed to have a broad-band overlap of the scattering cross section of even and odd multipoles in order to fulfill the GK condition as much as possible when it is immersed in water (Figure 1a). The spectrum of the efficiency for backscattering (EFB) is represented in Figure 1a and is equal to zero, whenever the GK condition is reached (see the Supporting Information for a definition of the EFB). We see that it reaches a minimum at three different positions, two of which reach the GK. As can be seen from the radiation diagrams taken at four specific wavelengths (Figure 1b), the scattering is predominantly forward, and the backscattering is nearly suppressed at the three wavelengths for which the EFB is minimal. At 425 and 615 nm, the superposition of odd and even multipoles is exact, and the GK condition is fulfilled. At 500 nm, even though the superposition is not exact, it is close enough that the GK condition is nearly reached. At 800 nm, however, the scattering cross section is dominated by the dipolar radiation of the nanocluster, and the radiation diagram is a torus centered around the direction of the electric dipole moment; and as a result, both forward and backward radiation occur. Thanks to the multipolar superposition, we further see in Figure 1c that the fraction of energy scattered in the forward direction is close to 1 over a broad range of wavelengths across the visible range, and following that metric, it does better than a high-index silicon nanosphere with a diameter equal to the external diameter of the dodecahedral cluster.

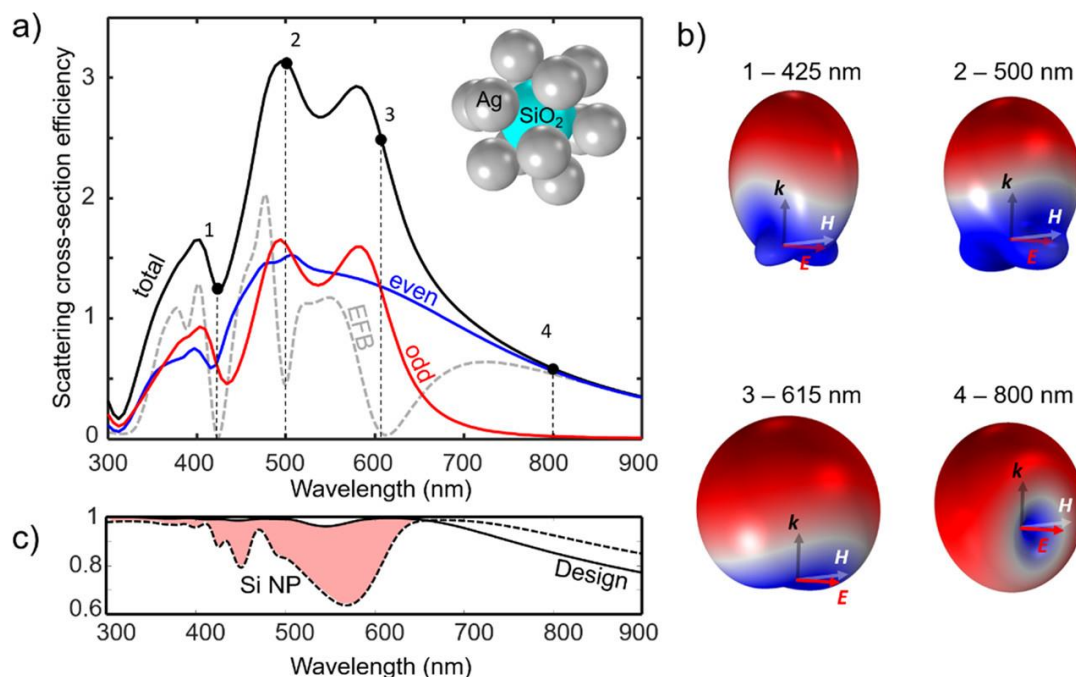


Figure 1. Designed dodecahedral nanocluster and scattering behavior. a) Scattering cross-section efficiency of the dodecahedral nanocluster as a function of wavelength. The red and blue lines evidence the contribution of the odd and even modes to the total scattering (black). The efficiency is defined as the scattering cross section divided by the outer geometrical

cross section of the particle: πR^2 , where R is the sum of the core radius, the satellite diameter, and the 0.5 nm spacer layer between the core and the satellites. The gray dashed curve is the efficiency for backscattering (EFB) spectrum. The inset is a 3D rendition of the designed dodecahedral nanocluster composed of a silica core surrounded by 12 silver satellites. b) Radiation diagrams of the modulus of the far field taken at the four spectral positions shown in panel a). The nanocluster is excited by a plane wave propagating in the direction of the propagation constant k (black arrow). The polarization directions of both the electric E (red arrow) and magnetic field H (white arrow) are shown for every diagram. c) Fraction of energy scattered in the forward direction as a function of wavelength for the designed dodecahedral nanocluster (continuous line) and for a silicon nanoparticle of radius equal to R .

We synthesized silver dodecapods by applying the principles of the fabrication of gold dodecahedral clusters presented in detail elsewhere.^(25,26) Briefly, a multistep synthetic process—which includes the fabrication of silica/polystyrene dodecahedral templates,^(27,28) the overgrowth of the silica core, the removal of the polystyrene satellites, and the regioselective functionalization of the concave dimples^(29–31)—enables the formation of silica particles with dodecahedrally coordinated concave dimples as shown in Figure 2a. The center of each dimple possesses an aminated polystyrene residue allowing attachment of 2–3 nm gold seeds (structure A_0). We developed a following one-step synthesis leading, in a few seconds, to the growth of silver directly on the dimpled templates. This synthesis protocol consists on successively adding a specific amount of silver nitrate, formaldehyde, and a solution of diluted ammonium hydroxide dropwise (detailed protocols in the Supporting Information). It is adapted from a previous protocol used to synthesize Ag nanoshells from silica particles decorated with gold seeds.⁽³²⁾ Formaldehyde starts a slow reduction of the silver onto the gold seeds attached in the dimples, and the pH increase, upon injection of sodium hydroxide, results in the Ag^+ ions reduction and their deposition onto the forming satellites. We synthesized batches with increasing satellite size (A_1 to A_{12} in Figures 2b and S1) by using different initial silver precursor amounts ($\times 1.5$ -fold between consecutive samples). The symmetrical spatial positioning of the 12 individual satellites onto the silica particles is confirmed by TEM images of well-orientated dodecapods (Figures 2a and S2). For low silver concentration (A_1 to A_3 in Figure 2b), each dimple is still composed of small individual Ag clusters. For higher concentration, the rather fast silver deposition provokes all the growing seeds to rapidly merge and form a single spheroidal Ag nanoparticle but still with traces of Au from the seeds at the bottom of the dimples (Figure 2c). The approach presented here offers several advantages compared to the synthesis of Au dodecapods.^(25,26) In those, gold satellites were grown by iteration directly on the dimpled templates, hence slower kinetics of the seed regrowth (hours compared to seconds). After the regrowth, each dimple was still filled with several individual gold nanoparticles. Therefore, a subsequent annealing step, after transfer into an organic solvent, was required to condense them into a larger single bulk Au nanoparticle which exhibited a lenslike shape.^(25,26) An additional oxidative etching of the gold could then be performed to make them spheroidal.⁽²⁶⁾ For silver, the growth conducted in one fast step avoids the dissolution of the fragile silica template in basic medium. Finally, as we shall see, the optical properties of the silver dodecahedra largely surpass those of gold, and the synthesis protocol offers unprecedented tunability of the multipolar response of odd parity modes with respect to even parity modes in the visible. We also observed that injecting the ammonium hydroxide directly, instead of dropwise, produced less spherical silver satellites resulting in weaker optical properties.

This approach takes advantage of several high-yield synthetic steps and results in the production of the plasmonic dodecapods, at the gram scale, with a yield as high as 70% (Figure 2d). The principal yield-limiting step is the synthesis of silica decorated with dodecahedrally coordinated polystyrene satellites, precursor of the silica particles with 12 dimples. We estimated the average satellite diameters of our samples by analyzing TEM images of the sample A_6 . It possesses individual Ag particles small enough to be well separated and therefore not overlapping on the EM images. Because only two or three pods can be precisely measured on a single dodecapod, the satellite size distribution obtained takes into account both the intra- and intersatellites variations. We found for A_6 an average radius of 27.4 ± 5.3 nm (Figure S3). Diameters of the other samples A_1 to A_{12} can be estimated from this single value because the silver amount increase of 1.5 is equivalent to a satellite diameter increase of $1.5^{1/3}$ (Table S1).

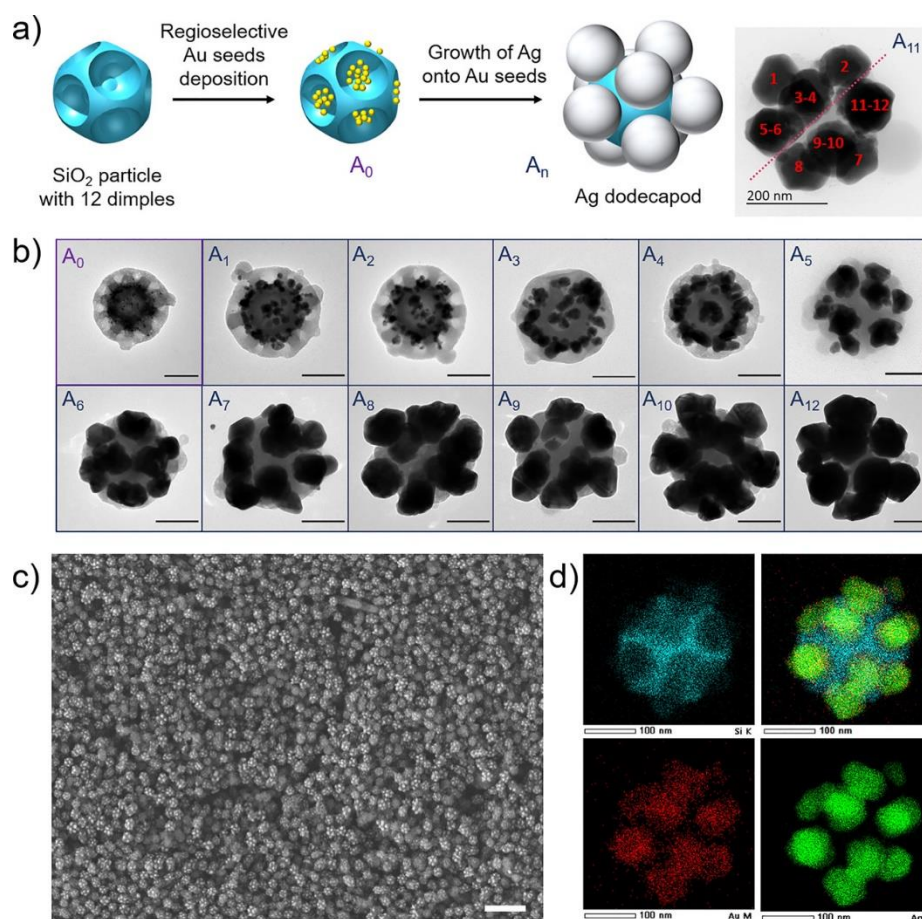


Figure 2. Silver dodecapods. *a)* Synthetic scheme of plasmonic clusters from a silica template with dodecahedrally coordinated dimples. Inset: bright-field TEM image exhibiting distinctively the 12 silver satellites. *b)* TEM close-ups of gold-seeded (A_0) and silver (A_1 to A_{12}) dodecapods with increasing silver satellites size. Scale bar = 100 nm. *c)* Widefield SEM image of silver dodecapods A_7 . Scale bar = 1 μm . *d)* STEM-EDX elemental analysis revealing silicon (top left), gold (bottom left), silver (bottom right), and overlaid view (top right) of the dodecahedral morphology.

The scattering properties of the dodecapods were studied using a polarization and angle-resolved static light scattering setup (SLS) described elsewhere.^(12,13) The linearly polarized white beam of a supercontinuum laser is shone onto a dilute suspension of dodecapods in water, and the scattered signal is collected and analyzed in polarization and energy by a microspectrophotometer. The scattering angle θ_{scat} can be set between 20 and 140° by a goniometric platform (Figure S4).

We first record the differential scattering at $\theta_{\text{scat}} = 90^\circ$ along the two output polarization channels parallel (σ_{\parallel}) and perpendicular (σ_{\perp}) to the scattering plane. The reason is that the scattering multipoles of order n split into two separate series when $\theta_{\text{scat}} = 90^\circ$; $\sigma_{\parallel}(90^\circ)$ collects the contributions of the modes of odd spatial parity, namely the magnetic and electric multipoles of odd and even order n , respectively, while $\sigma_{\perp}(90^\circ)$ collects the other modes of even spatial symmetry. Note that the forward scattering condition reads $\sigma_{\parallel}(180^\circ) = \sigma_{\perp}(180^\circ) = 0$. At dipolar order ($n = 1$) which may be a realistic approximation at the long-wavelength side of the resonance spectrum, $\sigma_{\parallel}(90^\circ)$ and $\sigma_{\perp}(90^\circ)$ measure the scattering from the magnetic (odd symmetry) and electric (even symmetry) dipoles, respectively, so that the first Kerker condition for forward scattering simply reads $\sigma_{\parallel}(90^\circ)/\sigma_{\perp}(90^\circ) = R_{M/E} = 1$. At shorter wavelengths, when higher order multipoles are excited and may overlap, the GK condition is more demanding as it involves all multipoles. The strict equality of the odd and even multipoles $a_n = b_n$ at each order n fully satisfies both the GK condition and the experimental equality $\sigma_{\parallel}(90^\circ)/\sigma_{\perp}(90^\circ) = 1$.⁽²⁴⁾ The GK condition is indeed less strict as it only requires the sum of the odd and even terms to be equal. Consequently, the ratio $\sigma_{\parallel}(90^\circ)/\sigma_{\perp}(90^\circ)$ may differ from 1 at the GK condition. However, we point out that this difference is expected to be weak, at least in the spectral region where the dipolar scattering is present. In other words, reaching values of the ratio $\sigma_{\parallel}(90^\circ)/\sigma_{\perp}(90^\circ)$ close to 1 at optical resonances augurs well for the production of intense Huygens' sources. Up to

now, the highest reported $R_{M/E}$ value for spherical scatterers is about 0.28 for plasmonic Ag raspberries.⁽¹³⁾ The parallel-to-transverse ratio $\sigma_{\parallel}(90^\circ)/\sigma_{\perp}(90^\circ)$ is plotted in Figure 3a across the visible spectrum.

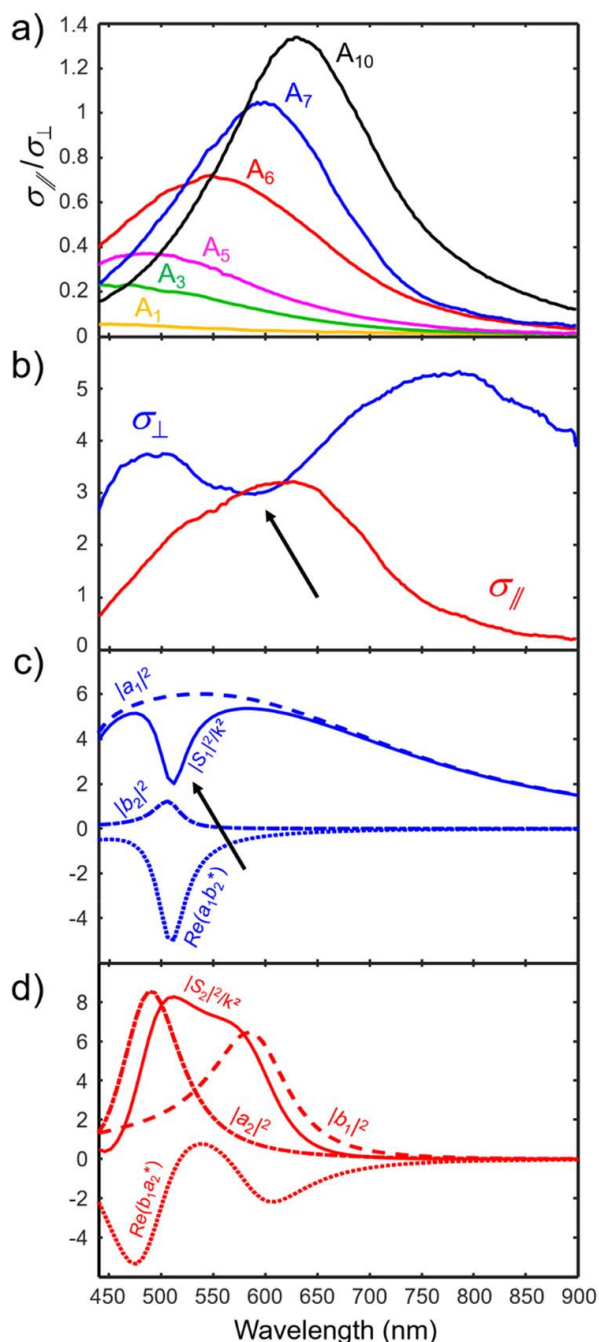


Figure 3. Optical properties of silver dodecapods. a) Spectral variations of $\sigma_{\parallel}(90^\circ)/\sigma_{\perp}(90^\circ)$ for samples within A_1 to A_{10} . b) Spectral variations of $\sigma_{\parallel}(90^\circ)$ in red and $\sigma_{\perp}(90^\circ)$ in blue for sample A_7 . c) Simulated spectral variations of $\sigma_{\perp}(90^\circ) = |S_1(\lambda)|^2/k^2$ (solid blue line) for the ideal dodecapod with dimensions corresponding to those of sample A_7 . Also represented are the contributions of the electric dipole ($|a_1|^2$), the magnetic quadrupole ($|b_2|^2$), and the interference term between the electric dipole and magnetic quadrupole ($\text{Re}(a_1 b_2^*)$). d) Simulated spectral variations of $\sigma_{\parallel}(90^\circ) = |S_2(\lambda)|^2/k^2$ (solid red line) for the ideal dodecapod with dimensions corresponding to those of sample A_7 . Also represented are the contributions of the magnetic dipole ($|b_1|^2$), the electric quadrupole ($|a_2|^2$), and the interference term between the magnetic dipole and electric quadrupole ($\text{Re}(b_1 a_2^*)$).

A series of broad bell-shaped curves are observed with a maximum that increases and red-shifts upon increasing the size of the silver satellites. The ratio $\sigma_{\parallel}(90^\circ)/\sigma_{\perp}(90^\circ)$ reaches 1 for A_7 and largely exceeds unity for A_{10} , hence surpassing previously reported values in a spectacular way.

The differential scattering cross sections $\sigma_{\parallel}(90^\circ)$ and $\sigma_{\perp}(90^\circ)$ can be extracted after proper normalization by a reference sample made of a suspension of calibrated polystyrene spheres (see the SI for details). The two components are shown in Figure 3b for sample A₇. The transverse signal $\sigma_{\perp}(90^\circ)$ shows a broad resonance at 600 nm, whereas the parallel signal $\sigma_{\parallel}(90^\circ)$ displays two maxima peaking at 500 and 775 nm and a clear dip is observed near 600 nm. At this stage, it is hard to assign these resonances to a particular set of scattering multipoles. We resort to numerical simulations of an ideal dodecapod with dimensions corresponding to those of sample A₇ to determine the multipolar contributions to the spectral behavior of $\sigma_{\perp}(90^\circ)$ and $\sigma_{\parallel}(90^\circ)$. $\sigma_{\perp}(90^\circ)$ and $\sigma_{\parallel}(90^\circ)$ are proportional to $|S_1(90^\circ)|^2/k^2$ and $|S_2(90^\circ)|^2/k^2$, respectively, where $S_1(90^\circ)$ and $S_2(90^\circ)$ are the scattering matrix amplitude coefficients at 90° (see the SI). Expressing these two quantities up to the quadrupolar multipolar terms enlightens the scattering behavior :

$$|S_1(90^\circ)|^2 = \frac{9}{4}|a_1|^2 + \frac{25}{4}|b_2|^2 + \frac{15}{2}\text{Re}(a_1b_2^*) + O(n > 2)$$

$$|S_2(90^\circ)|^2 = \frac{9}{4}|b_1|^2 + \frac{25}{4}|a_2|^2 + \frac{15}{2}\text{Re}(a_2b_1^*) + O(n > 2)$$

where a_1 (respectively b_1) is the electric (respectively magnetic) dipole coefficient, and a_2 (respectively b_2) is the electric (respectively magnetic) quadrupolar coefficient.

$O(n > 2)$ represents the multipolar terms of order higher than 2, which are fully considered in the numerical simulations. In this decomposition, a_1 and b_2 are the coefficients of the even multipoles, while b_1 and a_2 are the coefficients of the odd multipoles. Both $|S_1(90^\circ)|^2/k^2$ and $|S_2(90^\circ)|^2/k^2$ display the sum of three terms that contain the main contribution to the scattering: a dipole (a_1 or b_1), a quadrupole (a_2 or b_2), and an interference term between a dipole and a quadrupole (a_1 with b_2 or a_2 with b_1). The simulated spectral variations of $|S_1(90^\circ)|^2/k^2$ and $|S_2(90^\circ)|^2/k^2$ are represented on Figure 3c,d, along with the three leading terms contributing to the scattering. Both simulated curves reproduce the main features observed experimentally on the curves of $\sigma_{\parallel}(90^\circ)$ and $\sigma_{\perp}(90^\circ)$, albeit at different wavelengths, attributed to the polydisperse nature of the sample. We see that the dip observed for $\sigma_{\parallel}(90^\circ)$ is also present in $|S_1(90^\circ)|^2/k^2$ (pointed by a black arrow in Figure 3c) and is due to the interference between the electric dipole and magnetic quadrupole. We also see that $|S_2(90^\circ)|^2/k^2$ has a main resonance peak near the dip of $|S_1(90^\circ)|^2/k^2$ and is composed of a superposition of a magnetic dipole resonance and an electric quadrupole resonance. The interference term between these two multipoles reduces the amplitude of scattering at wavelengths below and above the main resonance peak of $|S_2(90^\circ)|^2/k^2$. These observations are a clear indication that the optical response of Ag dodecapods sits in an interference regime between odd and even multipoles.

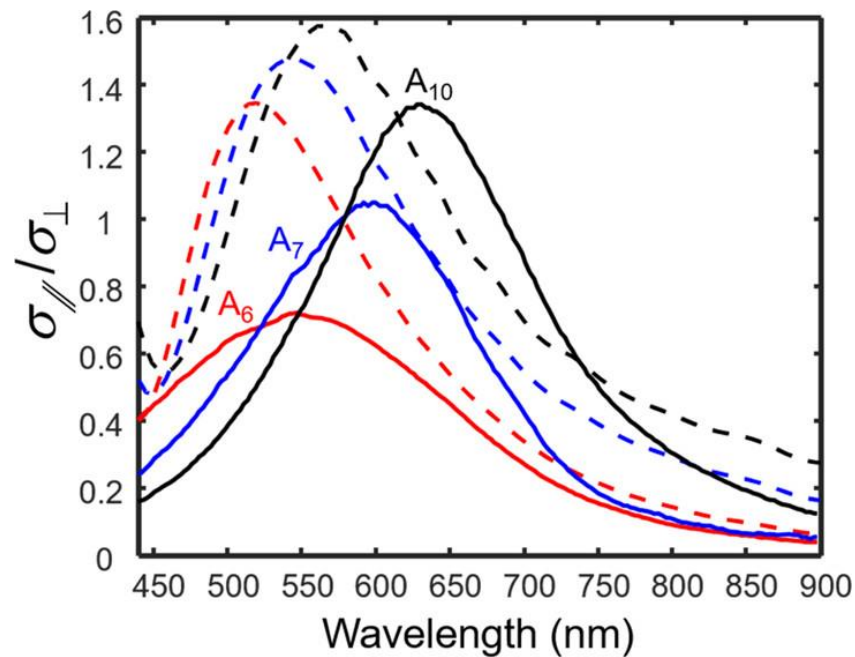


Figure 4. Comparison between simulations and experiment for samples A_6 , A_7 , and A_{10} . Solid curves are the experimental spectral variations of $\sigma_{\parallel}(90^\circ)/\sigma_{\perp}(90^\circ)$ for samples A_6 (red), A_7 (blue), and A_{10} (black). The dashed curves are the simulated $|S_2(\lambda)|^2/|S_1(\lambda)|^2$ for the corresponding dodecapod geometries taking the experimental polydispersity into account.

Figure 4 compares the experimental ratio $\sigma_{\parallel}(90^\circ)/\sigma_{\perp}(90^\circ)$ for samples A_6 , A_7 , and A_{10} to the simulated ratios $|S_2(\lambda)|^2/|S_1(\lambda)|^2$ for corresponding dodecapod dimensions and by considering the experimental polydispersity. The polydispersity for a given sample consists in a Gaussian distribution of the satellite size that follows the histogram of experimentally retrieved satellite sizes (see the SI for details). Experiments and simulations exhibit similar trends in terms of amplitude and frequency shift. Indeed, the amplitude of the ratio increases and red-shifts when the satellite size is increased. However, the resonance wavelengths are slightly different, and experimental data are systematically red-shifted compared to numerical simulations, suggesting a higher electromagnetic coupling between satellites in the real system. We assign this difference to the imperfect shape of the real satellites, which may grow bigger than the perfect spheres of the model while still not coalescing. Furthermore, the TEM images of Figure 2b reveal the presence of facets on the satellites, which, in turn, implies the presence of hot spots at the vertices. Both effects, bigger size and presence of hot spots, do enhance the electromagnetic coupling (as confirmed by UV-vis spectroscopy in Figure S5).

The equality of the parallel $\sigma_{\parallel}(90^\circ)$ and transverse $\sigma_{\perp}(90^\circ)$ scattering cross sections in sample A_7 together with the associated numerical simulations suggests that the optical response of these dodecapods may be close to the GK condition of forward-only scattering. In order to verify the directionality of the scattered light, we recorded the scattering across a broad range of angles θ_{scat} from 20° to 140° . Normalization with a reference suspension of polystyrene beads was used again for calibration. Figure 5a is a color plot of the measured total scattering (parallel + transverse) from sample A_7 as a function of wavelength and scattering angle. We see that the scattering is predominantly forward over a broad range of frequencies spanning almost all across the visible. Figures 5b are polar plots of the same data taken at three specific wavelengths (500 nm, 615 and 800 nm). The scattering is strongly forward for all three wavelengths. Moreover, the scattering strength and the forward directionality noticeably increased upon decreasing wavelength. Figure 5c shows the corresponding numerical simulations of the polar plots expected for the A_7 dodecapod system at the same three wavelengths, accounting for the polydispersity of the sample as for the simulations of Figure 4. The simulations reproduce remarkably well the experimental observation of the forward scattering increase both in strength and directionality upon decreasing wavelength. Interestingly, the experimental forward scattering appears to be squeezed in a narrower angular range than the simulated one. Once again, we ascribe this quantitative difference to the simplified description of the satellite shape and their polydispersity, particularly as it excludes dodecapods with too large silver satellites.

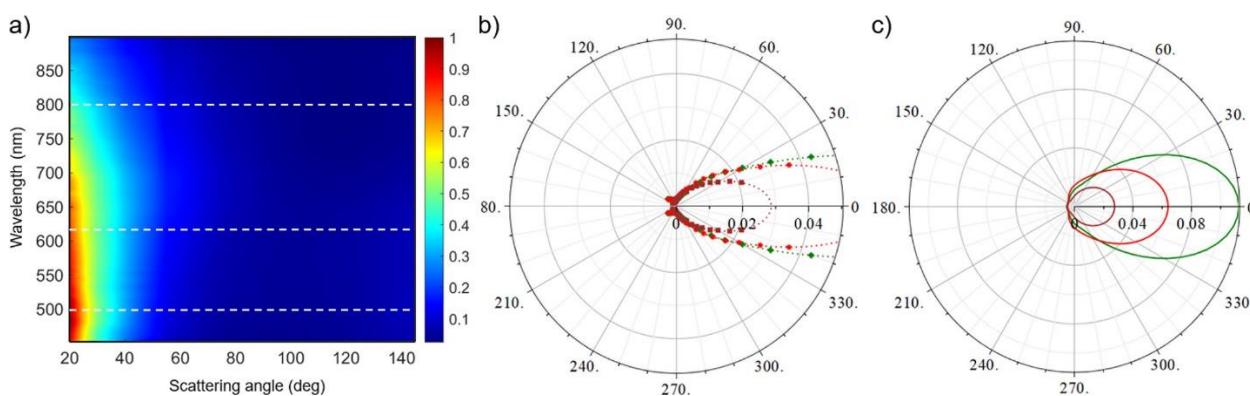


Figure 5. Ag dodecapod forward scattering. *a)* Color plot showing the measured scattered intensity as a function of the scattering angle and wavelength. The data are normalized to the maximum value. *(b and c):* Experimental *a)* and simulated *b)* scattering polar plots shown for sample A_7 at three wavelengths: 500 nm (green) 615 nm (red), and 800 nm (brown). The dashed lines on the color plot of panel *a)* show the wavelengths for which the polar plots are represented on panel *b)*. Symbols show actual data. The dotted lines are guides for the eyes computed as polynomials in $\mu = \cos \theta$ (see the SI for details).

In this work, we successfully synthesized dodecapods made of 12 silver satellites located at the faces of a dodecahedron. We demonstrated that, when the satellites are separated by nanoscale gaps, these finely engineered nanoclusters behave as powerful Huygens' sources in visible light: their scattering is strongly oriented toward the forward direction with a high scattering efficiency. Numerical simulations and experimental observations reveal that the scattering is not limited to dipolar order but results instead from the contribution of a series of electric and magnetic multipoles approaching the generalized Kerker condition that interfere. Our bottom-up approach enables to tune finely the size of the silver satellites and to produce large amounts of dodecapods with a high degree of control over morphology (with a yield of the same morphology as high as 70%). Our synthesis approach done in bulk can be scaled up, and the procedure could produce clusters at gram scales or more. This offers the possibility to make optical materials such as metasurfaces by depositing the structures on a bare or patterned substrate. This may contribute positively to the rationale behind metasurface fabrication because the individual Huygens' sources are designed and assembled separately from any substrate or array. In contrast to many top-down lithography techniques, they come in very large amounts, in the form of colloidal inks, which could be subsequently deposited or coated onto a surface to add functionality. Furthermore, since they are isotropic and resonant, the nanocolloidal platform could increase the potential of 3D metamaterials using hierarchical self-assembly.⁽¹³⁾

The Supporting Information is available free of charge at <https://pubs.acs.org/doi/10.1021/acs.nanolett.0c04666>.

- Materials and methods, electron microscopy, optical characterization, theoretical approach, and numerical simulations ([PDF](#))

Author Information

- Corresponding Authors :

- Mona Tréguer-Delapierre - Université de Bordeaux, CNRS, ICMCB, Bordeaux INP, UMR 5026, Pessac 33600, France; <http://orcid.org/0000-0002-3096-6645>; Email: mona.treguer@icmcb.cnrs.fr
- Alexandre Baron - Université de Bordeaux, CNRS, CRPP, UMR 5031, Pessac 33600, France; <http://orcid.org/0000-0003-0697-6410>; Email: alexandre.baron@u-bordeaux.fr

- Authors :

- Laurent Lermusiaux - Université de Bordeaux, CNRS, ICMCB, Bordeaux INP, UMR 5026, Pessac 33600, France; Present Address: Laboratoire de Chimie, CNRS, École Normale Supérieure de Lyon, 46 allée d'Italie, 69364 Lyon, France; <http://orcid.org/0000-0003-3024-0649>

- Véronique Many - Université de Bordeaux, CNRS, ICMCB, Bordeaux INP, UMR 5026, Pessac 33600, France; Université de Bordeaux, CNRS, CRPP, UMR 5031, Pessac 33600, France
- Philippe Barois - Université de Bordeaux, CNRS, CRPP, UMR 5031, Pessac 33600, France
- Virginie Ponsinet - Université de Bordeaux, CNRS, CRPP, UMR 5031, Pessac 33600, France
- Serge Ravaine - Université de Bordeaux, CNRS, CRPP, UMR 5031, Pessac 33600, France
- Etienne Duguet - Université de Bordeaux, CNRS, ICMCB, Bordeaux INP, UMR 5026, Pessac 33600, France; <http://orcid.org/0000-0002-0675-5987>

Funding : This work was supported by the LabEx AMADEus (ANR-10-LABX-42) and IdEx Bordeaux (ANR-10-IDEX-03-02), i.e., the Investissements d’Avenir program of the French government managed by the Agence Nationale de la Recherche.

Notes : The authors declare no competing financial interest.

Acknowledgments : TEM experiments were performed at the Plateforme de Caractérisation des Matériaux of the University of Bordeaux (UMS CNRS 3626). STEM and STEM-EDX experiments were performed at the Centre de Caractérisation R. Castaing of the University of Toulouse (UMS CNRS 3623).

Abbreviations : EM, Electron microscopy ; SLS, Static Ligth Scattering ; GK, Generalized Kerker ; EFB, Efficiency for Backscattering.

References :

- 1) Landau, L. D.; Lifshitz, E. M. *Electrodynamics of Continuous Media*; Pergamon Press: Oxford, 1960.
- 2) Pendry, J. B.; Holden, A. J.; Robbins, D. J.; Stewart, W. J. Magnetism from Conductors and Enhanced Nonlinear Phenomena. *IEEE Trans. Microwave Theory Tech.* **1999**, *47* (11), 2075– 2084, DOI: 10.1109/22.798002
- 3) Smith, D. R.; Padilla, W. J.; Vier, D. C.; Nemat-Nasser, S. C.; Schultz, S. Composite Medium with Simultaneously Negative Permeability and Permittivity. *Phys. Rev. Lett.* **2000**, *84* (18), 4184– 4187, DOI: 10.1103/PhysRevLett.84.4184
- 4) Alù, A.; Salandrino, A.; Engheta, N. Negative Effective Permeability and Left-Handed Materials at Optical Frequencies. *Opt. Express* **2006**, *14* (4), 1557– 1567, DOI: 10.1364/OE.14.001557
- 5) Alù, A.; Engheta, N. The Quest for Magnetic Plasmons at Optical Frequencies. *Opt. Express* **2009**, *17* (7), 5723– 5730, DOI: 10.1364/OE.17.005723
- 6) Rockstuhl, C.; Lederer, F.; Etrich, C.; Pertsch, T.; Scharf, T. Design of an Artificial Three-Dimensional Composite Metamaterial with Magnetic Resonances in the Visible Range of the Electromagnetic Spectrum. *Phys. Rev. Lett.* **2007**, *99* (1), 017401, DOI: 10.1103/PhysRevLett.99.017401
- 7) Simovski, C. R.; Tretyakov, S. A. Model of Isotropic Resonant Magnetism in the Visible Range Based on Core-Shell Clusters. *Phys. Rev. B: Condens. Matter Mater. Phys.* **2009**, *79* (4), 045111, DOI: 10.1103/PhysRevB.79.045111
- 8) Mühligh, S.; Cunningham, A.; Scheeler, S.; Pacholski, C.; Bürgi, T.; Rockstuhl, C.; Lederer, F. Self-Assembled Plasmonic Core-Shell Clusters with an Isotropic Magnetic Dipole Response in the Visible Range. *ACS Nano* **2011**, *5* (8), 6586– 6592, DOI: 10.1021/nn201969h
- 9) Dintinger, J.; Mühligh, S.; Rockstuhl, C.; Scharf, T. A Bottom-up Approach to Fabricate Optical Metamaterials by Self-Assembled Metallic Nanoparticles. *Opt. Mater. Express* **2012**, *2* (3), 269– 278, DOI: 10.1364/OME.2.000269

- 10) Sheikholeslami, S. N.; Alaeian, H.; Koh, A. L.; Dionne, J. A. A Metafluid Exhibiting Strong Optical Magnetism. *Nano Lett.* **2013**, *13* (9), 4137– 4141, DOI: 10.1021/nl401642z
- 11) Qian, Z.; Hastings, S. P.; Li, C.; Edward, B.; McGinn, C. K.; Engheta, N.; Fakhraai, Z.; Park, S.-J. Raspberry-like Metamolecules Exhibiting Strong Magnetic Resonances. *ACS Nano* **2015**, *9* (2), 1263– 1270, DOI: 10.1021/nn5050678
- 12) Ponsinet, V.; Barois, P.; Gali, S. M.; Richetti, P.; Salmon, J. B.; Vallecchi, A.; Albani, M.; Le Beulze, A.; Gomez-Grana, S.; Duguet, E.; Mornet, S.; Treguer-Delapierre, M. Resonant Isotropic Optical Magnetism of Plasmonic Nanoclusters in Visible Light. *Phys. Rev. B: Condens. Matter Mater. Phys.* **2015**, *92* (22), 220414, DOI: 10.1103/PhysRevB.92.220414
- 13) Gomez-Graña, S.; Beulze, A. L.; Treguer-Delapierre, M.; Mornet, S.; Duguet, E.; Grana, E.; Cloutet, E.; Hadziioannou, G.; Leng, J.; Salmon, J.-B.; Kravets, V. G.; Grigorenko, A. N.; Peyyety, N. A.; Ponsinet, V.; Richetti, P.; Baron, A.; Torrent, D.; Barois, P. Hierarchical Self-Assembly of a Bulk Metamaterial Enables Isotropic Magnetic Permeability at Optical Frequencies. *Mater. Horiz.* **2016**, *3* (6), 596– 601, DOI: 10.1039/C6MH00270F
- 14) Pfeiffer, C.; Grbic, A. Metamaterial Huygens' Surfaces: Tailoring Wave Fronts with Reflectionless Sheets. *Phys. Rev. Lett.* **2013**, *110* (19), 197401, DOI: 10.1103/PhysRevLett.110.197401
- 15) Mahmoud, A. M.; Engheta, N. Wave-Matter Interactions in Epsilon-and-Mu-near-Zero Structures. *Nat. Commun.* **2014**, *5* (1), 5638, DOI: 10.1038/ncomms6638
- 16) Kerker, M.; Wang, D.-S.; Giles, C. L. Electromagnetic Scattering by Magnetic Spheres. *J. Opt. Soc. Am.* **1983**, *73* (6), 765– 767, DOI: 10.1364/JOSA.73.000765
- 17) Dezert, R.; Richetti, P.; Baron, A. Isotropic Huygens Dipoles and Multipoles with Colloidal Particles. *Phys. Rev. B: Condens. Matter Mater. Phys.* **2017**, *96* (18), 180201, DOI: 10.1103/PhysRevB.96.180201
- 18) Elancheliyan, R.; Dezert, R.; Castano, S.; Bentaleb, A.; Nativ-Roth, E.; Regev, O.; Barois, P.; Baron, A.; Mondain-Monval, O.; Ponsinet, V. Tailored Self-Assembled Nanocolloidal Huygens Scatterers in the Visible. *Nanoscale* **2020**, *12* (47), 24177– 24187, DOI: 10.1039/D0NR05788F
- 19) Kruk, S.; Kivshar, Y. Functional Meta-Optics and Nanophotonics Governed by Mie Resonances. *ACS Photonics* **2017**, *4* (11), 2638– 2649, DOI: 10.1021/acsp Photonics.7b01038
- 20) Arbabi, A.; Horie, Y.; Ball, A. J.; Bagheri, M.; Faraon, A. Subwavelength-Thick Lenses with High Numerical Apertures and Large Efficiency Based on High-Contrast Transmitarrays. *Nat. Commun.* **2015**, *6* (1), 7069, DOI: 10.1038/ncomms8069
- 21) Yu, Y. F.; Zhu, A. Y.; Paniagua-Domínguez, R.; Fu, Y. H.; Luk'yanchuk, B.; Kuznetsov, A. I. High-Transmission Dielectric Metasurface with 2π Phase Control at Visible Wavelengths. *Laser Photonics Rev.* **2015**, *9* (4), 412– 418, DOI: 10.1002/lpor.201500041
- 22) Lin, D.; Fan, P.; Hasman, E.; Brongersma, M. L. Dielectric Gradient Metasurface Optical Elements. *Science* **2014**, *345* (6194), 298– 302, DOI: 10.1126/science.1253213
- 23) Chong, K. E.; Staude, I.; James, A.; Dominguez, J.; Liu, S.; Campione, S.; Subramania, G. S.; Luk, T. S.; Decker, M.; Neshev, D. N.; Brener, I.; Kivshar, Y. S. Polarization-Independent Silicon Metadevices for Efficient Optical Wavefront Control. *Nano Lett.* **2015**, *15* (8), 5369– 5374, DOI: 10.1021/acs.nanolett.5b01752
- 24) Dezert, R.; Richetti, P.; Baron, A. Complete Multipolar Description of Reflection and Transmission across a Metasurface for Perfect Absorption of Light. *Opt. Express* **2019**, *27* (19), 26317– 26330, DOI: 10.1364/OE.27.026317
- 25) Chomette, C.; Tréguer-Delapierre, M.; Schade, N. B.; Manoharan, V. N.; Lambert, O.; Taveau, J.-C.; Ravaine, S.; Duguet, E. Colloidal Alchemy: Conversion of Polystyrene Nanoclusters into Gold. *ChemNanoMat* **2017**, *3* (3), 160– 163, DOI: 10.1002/cnma.201600315
- 26) Many, V.; Dézert, R.; Duguet, E.; Baron, A.; Jangid, V.; Ponsinet, V.; Ravaine, S.; Richetti, P.; Barois, P.; Tréguer-Delapierre, M. High Optical Magnetism of Dodecahedral Plasmonic Meta-Atoms. *Nanophotonics* **2018**, *8* (4), 549– 558, DOI: 10.1515/nanoph-2018-0175

- 27) Perro, A.; Duguet, E.; Lambert, O.; Taveau, J.-C.; Bourgeat-Lami, E.; Ravaine, S. A Chemical Synthetic Route towards “Colloidal Molecules”. *Angew. Chem., Int. Ed.* **2009**, *48* (2), 361– 365, DOI: 10.1002/anie.200802562
- 28) Désert, A.; Chaduc, I.; Fouilloux, S.; Taveau, J.-C.; Lambert, O.; Lansalot, M.; Bourgeat-Lami, E.; Thill, A.; Spalla, O.; Ravaine, S.; Duguet, E. High-Yield Preparation of Polystyrene/Silica Clusters of Controlled Morphology. *Polym. Chem.* **2012**, *3* (5), 1130– 1132, DOI: 10.1039/c2py20058a
- 29) Désert, A.; Hubert, C.; Fu, Z.; Moulet, L.; Majimel, J.; Barboteau, P.; Thill, A.; Lansalot, M.; Bourgeat-Lami, E.; Duguet, E.; Ravaine, S. Synthesis and Site-Specific Functionalization of Tetravalent, Hexavalent, and Dodecavalent Silica Particles. *Angew. Chem., Int. Ed.* **2013**, *52* (42), 11068– 11072, DOI: 10.1002/anie.201304273
- 30) Hubert, C.; Chomette, C.; Désert, A.; Sun, M.; Treguer-Delapierre, M.; Mornet, S.; Perro, A.; Duguet, E.; Ravaine, S. Synthesis of Multivalent Silica Nanoparticles Combining Both Enthalpic and Entropic Patchiness. *Faraday Discuss.* **2015**, *181* (0), 139– 146, DOI: 10.1039/C4FD00241E
- 31) Chomette, C.; Duguet, E.; Mornet, S.; Yammine, E.; Manoharan, V. N.; Schade, N. B.; Hubert, C.; Ravaine, S.; Perro, A.; Tréguer-Delapierre, M. Templated Growth of Gold Satellites on Dimpled Silica Cores. *Faraday Discuss.* **2016**, *191* (0), 105– 116, DOI: 10.1039/C6FD00022C
- 32) Jackson, J. B.; Halas, N. J. Silver Nanoshells: Variations in Morphologies and Optical Properties. *J. Phys. Chem. B* **2001**, *105* (14), 2743– 2746, DOI: 10.1021/jp003868k